

## Porosity and free gas estimates from controlled source electromagnetic data at the Scanner Pockmark in the North Sea

Romina A.S. Gehrman<sup>a,\*</sup>, Giuseppe Provenzano<sup>a,e</sup>, Christoph Böttner<sup>b,f</sup>, Héctor Marín-Moreno<sup>c,g</sup>, Gaye Bayrakci<sup>c</sup>, Yee Y. Tan<sup>a</sup>, Naima K. Yilo<sup>a</sup>, Axel T. Djanni<sup>a</sup>, Karen A. Weitemeyer<sup>a,h</sup>, Timothy A. Minshull<sup>a</sup>, Jonathan M. Bull<sup>a</sup>, Jens Karstens<sup>b</sup>, Christian Berndt<sup>b</sup>

<sup>a</sup> University of Southampton, School of Ocean and Earth Science, National Oceanography Centre Southampton, UK

<sup>b</sup> GEOMAR, Helmholtz Centre for Ocean Research Kiel, Germany

<sup>c</sup> National Oceanography Centre, Southampton, UK

<sup>d</sup> Dalhousie University, Department of Oceanography, Halifax, NS, Canada

<sup>e</sup> Institut des Sciences de la Terre, Université Grenoble Alpes, Grenoble, France

<sup>f</sup> Kiel University, Marine Geophysics and Hydroacoustics, Kiel, Germany

<sup>g</sup> Norwegian Geotechnical Institute, Oslo, Norway

<sup>h</sup> Ocean Floor Geophysics Ltd, Vancouver, Canada

### ARTICLE INFO

#### Keywords:

North Sea  
Fluid pathway  
Electromagnetics  
Physical properties  
Resistivity  
Seismic reflection

### ABSTRACT

We present porosity and free gas estimates and their uncertainties at an active methane venting site in the UK sector of the North Sea. We performed a multi-disciplinary experiment at the Scanner Pockmark area in about 150 m water depth to investigate the physical properties of fluid flow structures within unconsolidated glacio-marine sediments. Here, we focus on the towed controlled source electromagnetic (CSEM) data analysis with constraints from seismic reflection and core logging data. Inferred background resistivity values vary between 0.6–1  $\Omega\text{m}$  at the surface and 1.9–2.4  $\Omega\text{m}$  at 150 mbsf. We calibrate Archie's parameters with measurements on cores, and estimate porosities of about  $50 \pm 10\%$  at the seafloor decreasing to  $25 \pm 3\%$  at 150 mbsf which matches variations expected for mechanical compaction of clay rich sediments. High reflectivity in seismic reflection data is consistent with the existence of a gas pocket. A synthetic study of varying gas content in this gas pocket shows that at least  $33 \pm 8\%$  of free gas is required to cause a distinct CSEM data anomaly. Real data inversions with seismic constraints support the presence of up to  $34 \pm 14\%$  free gas in a 30–40 m thick gas pocket underneath the pockmark within the stratigraphic highs of a till layer above the glacial unconformity in the Aberdeen Ground Formation.

### 1. Introduction

The controlled source electromagnetic (CSEM) method can be used as a powerful constraint on the electrical resistivity of the subsurface, which in the case of marine sediments is largely controlled by sediment porosity and pore fluid composition (e.g., Edwards, 2005). Here, we present porosity and free gas concentration estimates for the first 200 m of unconsolidated sediments at the Scanner Pockmark in the UK licensing block 15/25 in the North Sea (Fig. 1).

Our CSEM experiment forms part of a multidisciplinary study (Robinson et al., 2021) to assess the role of vertical/sub-vertical fluid

conduits in the integrity of carbon storage sites. Offshore carbon storage sites currently encompass reservoir rocks that are typically a couple of kilometres below the seafloor and are sealed with low-permeability cap rocks, such as the proposed Golden Eye (Dean and Tucker, 2017) and the active Sleipner (e.g., Boait et al., 2012) sites. To ensure the safety of carbon storage sites, assessment of the cap rock on a larger regional scale is required. For example, Karstens and Berndt, (2015) mapped vertical fluid conduits that potentially connect deeper stratigraphic layers with the sediment overburden about 10 km from Sleipner, and it is therefore important to understand the nature of these conduits.

Focused fluid conduits often show anomalies on seismic images with

\* Corresponding author at: University of Southampton, School of Ocean and Earth Science, National Oceanography Centre Southampton, UK.

E-mail address: [R.A.Gehrman@soton.ac.uk](mailto:R.A.Gehrman@soton.ac.uk) (R.A.S. Gehrman).

<https://doi.org/10.1016/j.ijggc.2021.103343>

Received 15 September 2020; Received in revised form 20 March 2021; Accepted 20 April 2021

Available online 12 May 2021

1750-5836/© 2021 Elsevier Ltd. All rights reserved.

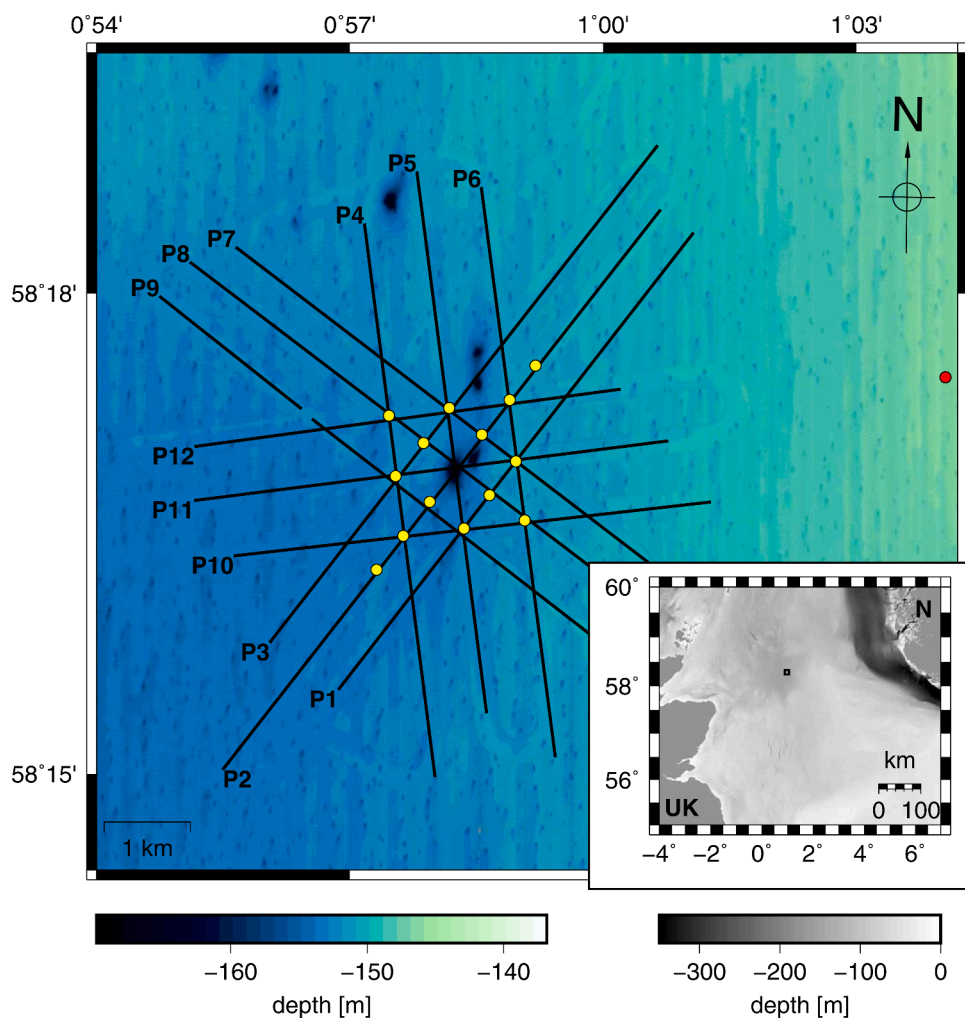


**Fig. 1.** Ship bathymetry at Scanner Pockmark Complex located between the UK and Norway (N) in the Central North Sea (position indicated with rectangle in inset). Collocated CSEM and seismic reflection profiles from cruise MSM63 (Berndt et al., 2017) are marked as black lines, and CSEM ocean bottom instruments as yellow dots. The Rock Drill 2 reference drill site from cruise MSM78 (Karstens et al., 2019) is shown as a red dot about 6 km to the East of the CSEM survey. (For interpretation of the references to colour in this figure legend, the reader is referred to the web version of this article.)

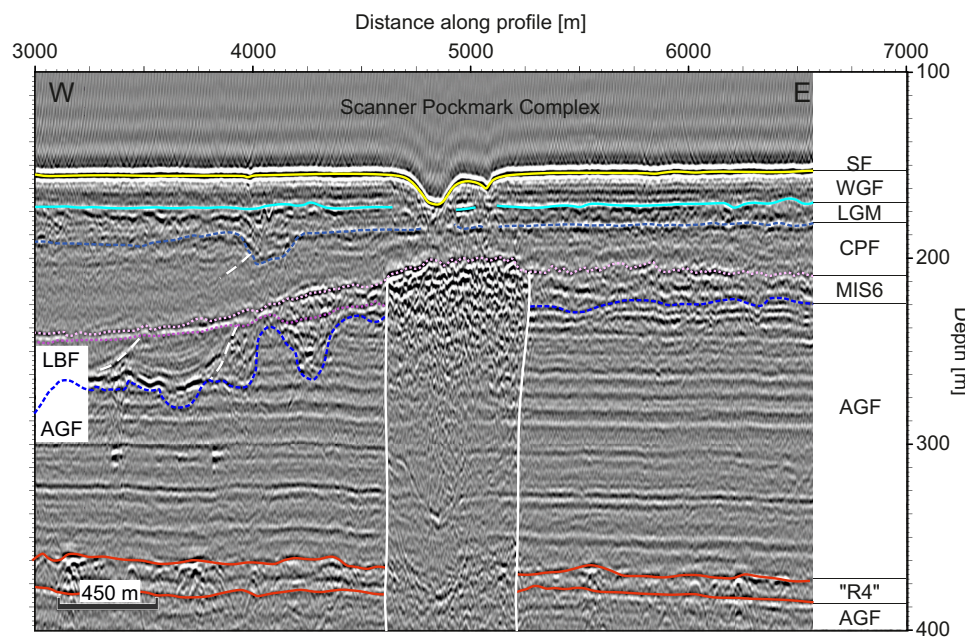


**Fig. 2.** Seismic section across the Scanner Pockmark Complex collocated with CSEM profile P11 (Fig. 1) and main stratigraphic units. Underneath the seafloor (SF, yellow line) lies the Witch Ground Formation (WGF, down to cyan line) and then the Swatchway Formation of the last glacial maximum (LGM, dashed light blue line). Sediments in these top units transition from marine with observed horizontal layering to glaciomarine to glacial deposits with interrupted layering. Below lies the Coal Pit Formation (CPF, a seismically transparent unit, above the top of the MIS 6 till unit (dashed purple line) and the Ling Bank Formation (LBF, filling tunnel valleys). The white lines border the approximate outline of the chimney that is characterised by a bright spot at the top of MIS 6, seismic blanking beneath and discontinuities in the sediment layering in the Aberdeen Ground Formation (AGF, Stoker et al. (2011)). Layering of the AGF is interrupted with the Mid Pleistocene Transition unit "R4" (red lines, Reinardy et al., 2017). (For interpretation of the references to colour in this figure legend, the reader is referred to the web version of this article.)

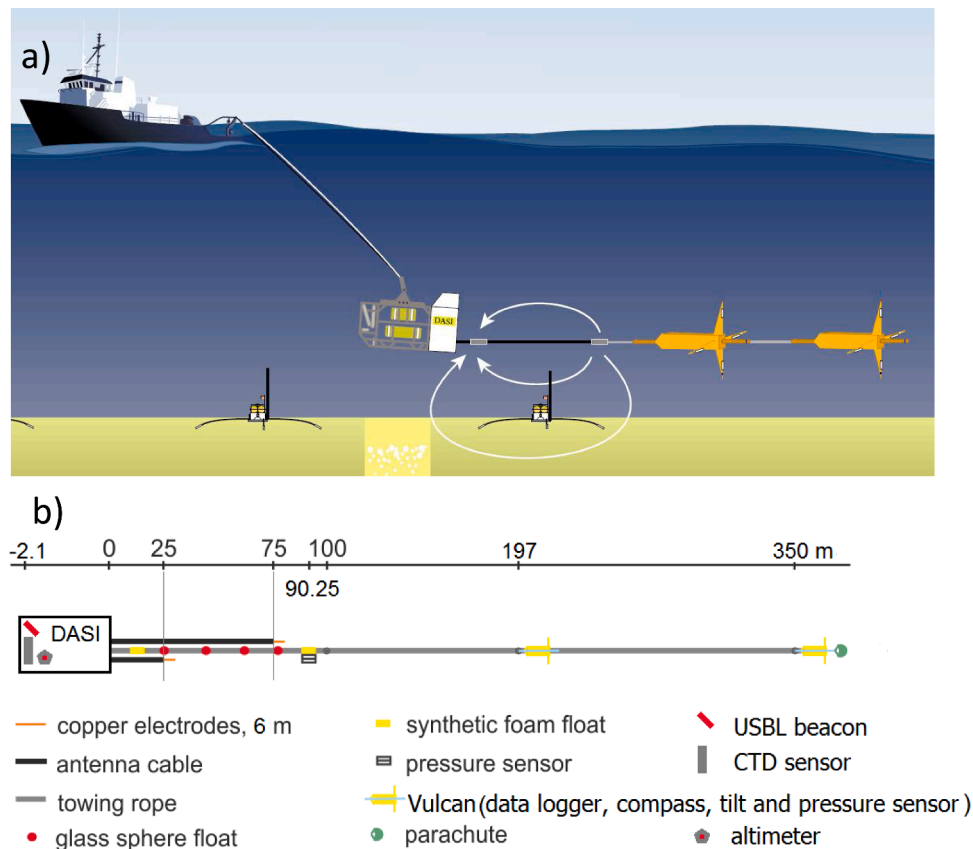


**Fig. 3.** (a) Sketch of the survey instrumentation including the electromagnetic source DASI towing the 50-m long antenna (current stream lines are white), and the two Vulcan three-axis electric field receivers, and three-axis electric field ocean bottom receivers across an active venting site (free gas as white bubbles); (b) Sketch of DASI-antenna-Vulcan setup with equipment distances. Instrument size not to scale.

vertical zones of chaotic reflections, dimmed or wiped-out zones, and bright spots (strong phase reversed reflectors, e.g., White, 1975) at different stratigraphic levels (Andresen, 2012; Cartwright et al., 2007; Løseth et al., 2009). Vertical fluid conduits can be active as short-term blow-out events (e.g., resulting in pipe structures offshore Norway, Bünz et al., 2003), or have long-lasting and continuous fluid flow (e.g., the chimney structures above the leaking hydrocarbon reservoir Tommeliten, Arntsen et al., 2007).

Our study area is the Scanner Pockmark site in the Witch Ground Basin and contains a large number of seafloor depressions (two distinct classes of pockmarks, Böttner et al., 2019; Gafeira and Long, 2015), of which the large class 1 pockmarks (more than 15 m deep) are related to active ebullition of methane across the seabed (Judd et al., 1994). Sediment deposition in the Witch Ground Basin involves mostly fine-grained material and was rapid during the end of the last glacial period between 15 and 13 ka. Since 8 ka the area was affected very little by erosion or sedimentation, but methane gas venting from underlying strata was likely active (Hovland and Sommerville, 1985; Judd et al., 1994). In the depths reached by our study (about 150 to 200 mbsf) the following stratigraphic units are identified (Fig. 2) by Stoker et al. (2011) and Böttner et al. (2019): At depth, the Aberdeen Ground Formation (AGF) is a thick basal Quaternary unit with clay-rich layered sediments, whose top represents a regional glacial unconformity. The AGF is interrupted by the Mid Pleistocene Transition (“R4” Reinardy et al., 2017) at about ~390 mbsf, whose high amplitude reflection suggest the presence of free gas (Böttner et al., 2019). Tunnel valleys cutting into the AGF are part of the Ling Bank Formation (LBF, Marine Isotope Stage MIS 10–12, 374–478 ka). Above the AGF and LBF, an interval of glacial till deposits (MIS 6, 191 ka) with interrupted layering and variable thickness laterally is thought to act as an intermediate

reservoir for shallow gas. The Coal Pit Formation (MIS 3–6, 57–191 ka) is composed of fine-grained glacial tills with transparent to chaotic seismic facies that contrast with the MIS 6 deposits. It transitions into the finely laminated seismic reflections of the Swatchway Formation, which were deposited during the last glacial maximum (LGM, start of MIS 2). The lower Witch Ground Formation (WGF) is composed of glacial to glaciomarine sediments and characterised by interrupted layering. The shallowest stratigraphic unit is the upper WGF composed of horizontally layered glaciomarine to marine sediments of late Pleistocene to Holocene age (MIS 1–2, 14–29 ka). The WGF is mostly eroded at the Scanner Pockmark.

We interpret the physical properties of the unconsolidated, glaciomarine sediments in terms of porosity and gas concentrations and their associated uncertainties. Our approach is to calibrate a rock physics (Archie, 1942) relationship with core logging data to convert resistivity models inferred from CSEM data to porosity. We compare resistivity-derived porosities to trends from mechanical compaction to investigate the dominant factors controlling porosity changes with depth in our study area. To estimate free gas concentrations underneath bright spots observed in the seismic reflection data, we add stratigraphic constraints from the seismic reflection data to the resistivity model. The inferred resistivities are converted to free gas content using Archie’s relationship accounting for the uncertainty of each parameter. We also run a synthetic data study to analyse the sensitivity of the CSEM data to free gas abundance. Free gas occurrences are then interpreted in the geological context and contribute to the multidisciplinary analysis (e.g., seismic properties, fluid flow modelling) of the Scanner Pockmark site and to the understanding of the system dynamics (fluid flow cycle, accumulations of free gas in stratigraphic layers, chemistry exchange).

## 2. Geophysical data analysis

During cruise MSM63 (Berndt et al., 2017) controlled source electromagnetic (CSEM) and active seismic experiments were conducted to analyse the physical properties of the Scanner Pockmark Complex. Combined analysis of the two complementary techniques have been shown to improve the interpretation of the pore fluid composition (e.g., Gehrman et al., 2019; Goswami et al., 2015; Kannberg and Constable, 2020; Schwalenberg et al., 2020; Weitemeyer et al., 2011). While seismic reflection data have a much higher resolution to structural changes, CSEM data are especially sensitive to the pore fluid. For example, a few per cent of free gas in the pore space may cause seismic bright spots but only a small response in the CSEM data, while larger amounts of free gas cause no significant additional change in the seismic data, but a strong response in the CSEM data (Constable, 2010). Therefore, CSEM and seismic methods complement each other, and CSEM is a powerful tool for hydrocarbon (e.g., MacGregor et al., 2006), fluid flow (e.g., Naif et al., 2015), groundwater (e.g., Gustafson et al., 2019; Haroon et al., 2018; Micallef et al., 2020), active pockmarks (Goswami et al., 2017) and carbon storage (e.g., Morten and Bjørke, 2020; Park et al., 2017) studies.

The CSEM experiment at the Scanner Pockmark complex encompassed the Deep-towed Active Source Instrument (DASI, Sinha et al., 1990), two towed electric field receivers (Vulcan, Constable et al., 2016) and 14 ocean bottom instruments from the UK Ocean Bottom Instrument Facility (Fig. 3, Minshull et al., 2005). The electromagnetic source DASI was powered from the ship through a deep-tow cable. The source emitted an up to 110 A square-wave signal with a fundamental frequency of 1 Hz (the fundamental and the first three odd harmonics are chosen for analysis, see Section 2.2) from a nearly neutrally-buoyant, 50 m-long antenna.

Here, we present the analysis of the data recorded with the two three-axis Vulcan receivers (Constable et al., 2016) towed behind DASI at 197 and 350 m offset (Fig. 3). The CSEM survey was carried out about 20–40 m above the seafloor. The instrument array was towed along twelve profiles in a star pattern across the pockmark at four azimuths (Fig. 1).

### 2.1. CSEM data processing

The transmitter and receiver data are processed profile by profile for odd harmonic frequencies from the fundamental frequency of 1 Hz up. The raw time series are transformed to the frequency domain by applying a Fast Fourier Transform using 1-s long time windows (one period of the square wave signal). The receiver data are then corrected for their frequency-dependent, complex amplifier response function and normalised by the receiver dipole length. The Earth response  $C(f)$  is calculated by dividing the receiver response  $R(f)$  by the source dipole moment  $S(f)$  for each frequency:  $C(f) = R(f)/S(f)$  (adapting the routine of Myer et al., 2011). Preliminary analysis of the horizontal electric field  $E_y$  data ( $y$  is defined being in-line with the tow direction and the ideal orientation of the source dipole) of both receivers show lower amplitudes than expected, suggesting the possibility of damaged electrodes leading to an equivalent hardware high-pass filtering effect. We, therefore, use the vertical electric field  $E_z$  data only. Note, that the 1 m-long vertical antenna of the Vulcan was never in a true vertical position, due to the movement in the water column (and resulting change of instrument pitch), and contains a small part of the  $E_y$  signal.

A drift of internal quartz clocks compared to the GPS time was noticed in both receivers after instrument recovery. The data are corrected for this clock drift. Preliminary data analysis suggests that an additional time delay is required to match the phase data. Given this timing uncertainty, we base the interpretations in this paper on

amplitudes only but discuss the time delay in Appendix A.

Finally, responses within 30-s long time windows are stacked to improve the signal-to-noise ratio and to estimate a data error from the standard deviation of the stacks. Additionally, navigational uncertainties are estimated using a 2D perturbation study (Gehrman et al., 2019b), which are added in quadrature to the data errors from the stacking process, and result in a few per cent error for the closest Vulcan and about ten per cent error for the furthest Vulcan.

### 2.2. Air-water boundary effects and choice of frequency range

The time-varying electric current transmitted by a horizontal dipole source causes electromagnetic energy to be coupled inductively perpendicular to the direction of propagation, in the horizontal plane, and galvanically in direction of propagation, in the vertical plane. In water depths less than the receiver offset, a significant amount of the electromagnetic energy measured is guided along the air-water boundary, which due to the large resistivity of the air layer is dominated by inductive coupling (Chave and Cox, 1982). The energy travelling along the air-water boundary has, therefore, no vertical component, so that ideally for a vertical dipole  $E_z$  consists solely of energy that has travelled through the seabed and sea water. In contrast, the measured horizontal component contains a large amount of energy that has travelled along the air-water boundary due to its amplitude decaying only with  $1/r$ , where  $r$  is the receiver-source offset. In comparison, the energy that travels through the seabed decays exponentially (Weidelt, 2007).

In the measured  $E_z$  data, we observe frequencies with high signal-to-noise ratios up to 127 Hz that could potentially be used in the data inversion. Generally, the square wave transmitted has the highest energy in the base frequency (here, 1 Hz) and then falls off as  $1/n$ , where  $n$  is the harmonic number. Higher frequencies often exhibit a smaller signal-to-noise ratio with increasing offset (Myer et al., 2011), and are less sensitive to deeper structure in the seabed (see for example Andréis and MacGregor, 2008). To decide how many frequencies and which range of frequencies to use, we ran simulations using the forward modelling code in MARE2DEM (Key, 2016) for a simple model with increasing resistivities with depth and with and without a resistive gas pocket at about 40 mbsf (Fig. 4a). The resistive gas pocket causes the simulated data for  $E_z$  at 5 Hz at 350 m offset (Fig. 4b, top) to be recognisably different (data difference above the data error from the navigational perturbation study, Fig. 4b, middle). In fact, the data anomaly, the absolute differences between these two synthetic data sets, for 0% and 40% free gas respectively, divided by the data error (Fig. 4b, bottom), is larger than one at several locations along the profile. The data anomaly is largest for the low to intermediate frequency range (around 7 Hz, Fig. 4c and d). The data anomaly pattern varies most with frequency below 7 Hz, while the shape of the anomaly for 350 m offset varies little above  $\sim 7$  Hz (Fig. 4d, supplementary material S.1). The latter suggests that frequencies above 7 Hz contain similar information about the subsurface to frequencies below 7 Hz. Including data of several high frequencies into an inversion therefore introduces a bias towards the higher frequencies. For the shorter offset (197 m), the data anomaly seems more variable for higher frequencies (Fig. 4c), but the data itself become more sensitive to the topography and less to the subsurface structure. An example of an inversion using a different range of frequencies can be found in the supplementary material S.2.

We decided to run inversions for frequencies of 1–7 Hz due to the greater variation in the pattern of data anomalies compared to higher frequency ranges, lower frequencies containing more information on deeper structure, and because the frequency range potentially covers the largest anomalies caused by a resistive gas pocket.

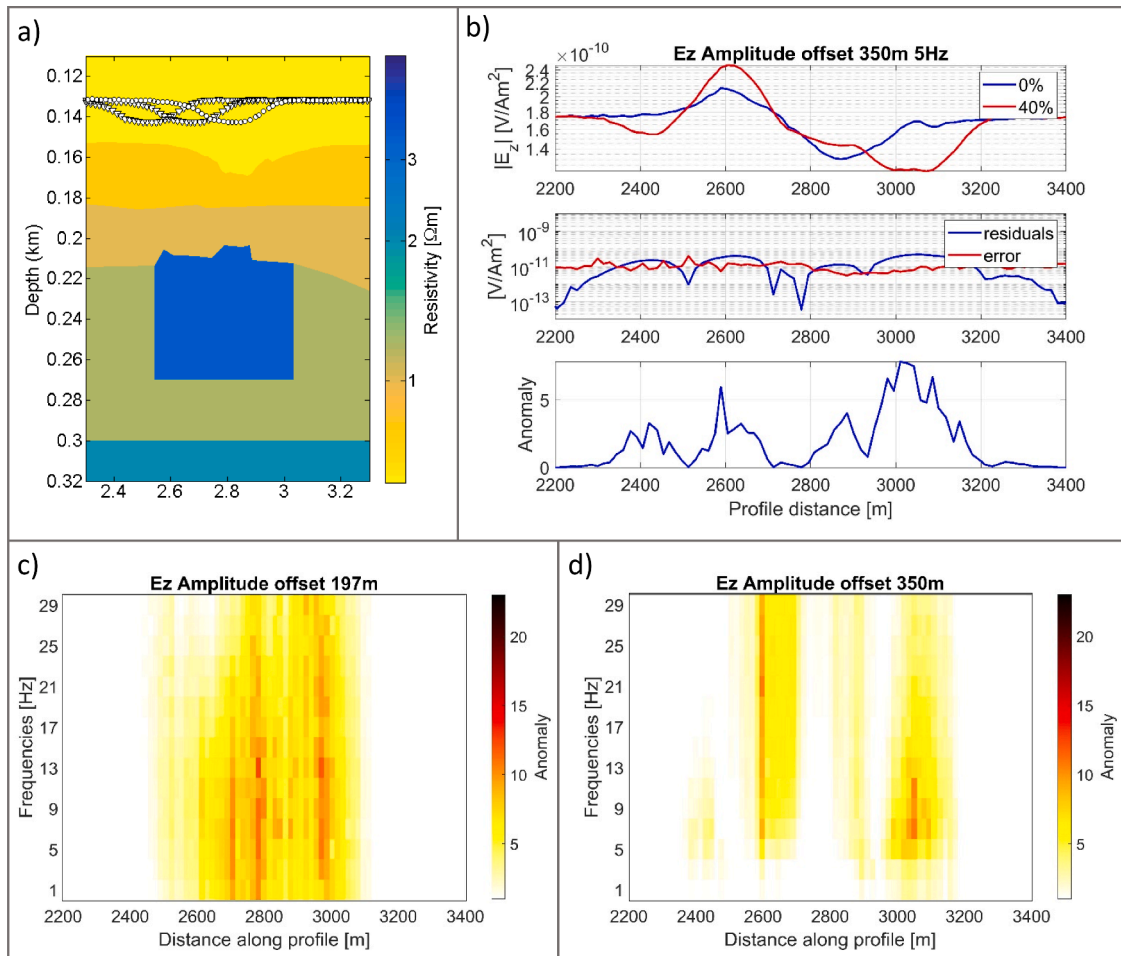


**Fig. 4.** (a) Model with gas pocket; (b) Top: Example of synthetic vertical electric field  $E_z$  data at 5 Hz for zero and 40% free gas in gas pocket (shown in a); (b) Middle: Absolute difference between the synthetic data (blue line, residuals) compared to realistic data errors (red line); (b) Bottom: Resulting data anomaly (residuals divided by data errors); (c and d) Data anomaly for synthetic data with and without gas pocket across the pockmark (centred at profile km 2.8) for 1 to 31 Hz for the nearest (c) and the furthest (d) Vulcan. (For interpretation of the references to colour in this figure legend, the reader is referred to the web version of this article.)

### 2.3. Seismic reflection data analysis

High-resolution reflection 2-D multi-channel seismic (MCS) data have been acquired in lines coincident with the CSEM experiment. An array of two GI-guns of 210 cubic inches each operating in harmonic mode, towed at 2 m depth below the sea surface, was fired with a shot interval ranging between 10.5 and 15 m. The reflected wavefield was detected by a 150 m-long streamer with 96 channels and a 1.5625 m group spacing. Depth controllers fixed the streamer depth to 2 m below sea surface.

On-board processing of the MCS data included geometry and source-receiver delay corrections, static corrections, common-depth-point (CDP) binning to 1.5625 m, and minimum-phase frequency bandpass filtering with corner frequencies of 25, 45, 420, 500 Hz. A normal move-out correction was applied to CDP gathers, using a simple velocity model of 1488 m/s in the water column (based on sound velocity profiling) and 1500 m/s in the sub-seabed, which is expected to sensibly correct the wavefield kinematics in the shallow water-saturated subsurface. On-board processing was completed by CDP-stacking and post-stack 2-D Stolt migration (Stolt, 1978). The expected  $\lambda/4$  tuning thickness resolution (Kallweit and Wood, 1982) is in the order of 2.5 m, based on a dominant post-stack frequency of 150 Hz (Berndt et al., 2017).

Post-stack processing included predictive deconvolution to reduce the wavelet duration, and predictive multiple attenuation (Peacock and Treitel, 1969), to eliminate the seafloor reverberation overprinting the subsurface reflections with a period of ca. 200 ms. Finally, the data were

converted from two-way-traveltime to depth with a smooth 2D velocity model, to use them as a constraint for CSEM resistivity inversion.

### 2.4. CSEM data inversion

Isotropic resistivity models were obtained using the 2.5-D inversion algorithm MARE2DEM (Key, 2016). The algorithm minimizes the functional

$$U = \| \mathbf{Rm} \|^2 + \mu \| \mathbf{W}(\mathbf{d} - F(\mathbf{m})) \|^2, \quad (1)$$

where the first term is a measure of the model roughness depending on the contrasts between model cells  $\mathbf{m}$ , here the logarithm of the resistivity bound between 0.1 and 200  $\Omega\text{m}$ . The second term measures the data fit, the difference between the observed data  $\mathbf{d}$  and the predicted data  $F(\mathbf{m})$  weighted by  $\mathbf{W}$ , a diagonal matrix containing the inverses of the data errors. The trade-off between model roughness and the data fit depends on the data errors and on the Lagrange multiplier  $\mu$ , which is estimated intrinsically throughout the inversion. The inversion is based on Occam's razor (Constable et al., 1987), so that the "simplest", in this case, least rough model, is preferred. The roughness term stabilizes the inversion so that spurious structures are not introduced into the over-parameterised model. Here, an  $L_2$  norm of the model gradient is approximated, also taking into account the distance to neighbouring cells as well as their area (see eq. 34 in Key, 2016), resulting in smaller resistivity contrasts for smaller cells. The optimal model is found by an

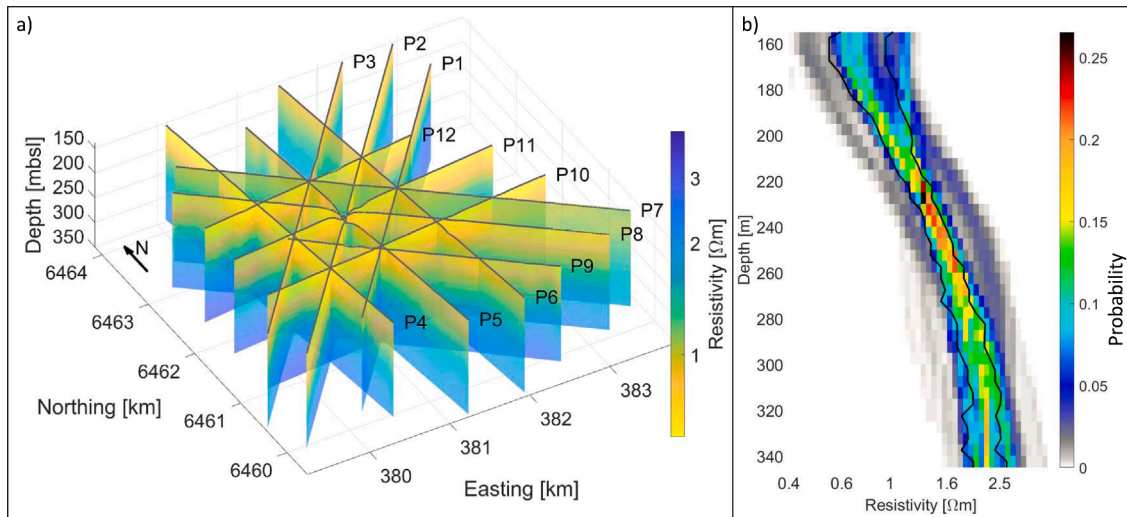


**Fig. 5.** (a) Unconstrained resistivity models for all twelve profiles from 2D data inversion; (b) Background resistivity probability distribution from resistivity profiles P1–P12 in (a) with one standard deviation indicated by black lines.

iterative process that linearises the functional  $U$  around the current model and then gradually updates it using the Jacobian matrix  $\mathbf{J}$ , with data sensitivities  $J_{ij} = \partial F_i(\mathbf{m}) / \partial m_j$ .

The chosen starting models were half spaces with a resistivity of 1  $\Omega\text{m}$ . The final models have a root mean square data misfit (the square root of the data fit in eq. 1 divided by the number of data) close to one. They seem robust against the choice of starting model: for example, a test with a 10  $\Omega\text{m}$ -halfspace starting model for profile P5 just results in an increase in the number of iterations from four to six. Resistivity models for twelve profiles (Fig. 5) using Vulcan  $E_z$  amplitude data for 1, 3, 5, and 7 Hz show an increase of resistivity with depth from 0.6–1  $\Omega\text{m}$  at the surface to 2–2.6  $\Omega\text{m}$  at 200 mbsf. The data presented here can be fully explained within the data errors by an isotropic model and inversions incorporating anisotropy between horizontal and vertical resistivity also converge to an isotropic model.

### 3. Porosity estimation from resistivity and sediment compaction trend

Resistivity can be related to porosity using the empirical Archie's relationship (Archie, 1942; Hearst et al., 2000). The logarithmic expression of Archie's relationship, relating the ratio between the bulk (b) and the fluid (f) resistivity  $\rho$  to the porosity  $\phi$  assuming water-saturated sediments,

$$\log_{10}(\rho_b / \rho_f) = \log_{10} a - m \log_{10} \phi \quad (2)$$

plots in a straight line (Pearson et al., 1983). Archie's parameters  $a$  and  $m$  depend on pore connectivity and clay content among other factors. The cementation factor  $m$  increases from unconsolidated to cemented sediments.

To calibrate Archie's parameters, we use porosity and resistivity data acquired with the multi-sensor core logger (MSCL) at the British Ocean Sediment Core Research Facility (BOSCORF) on cores from a reference site 6 km to the North East of the pockmark and away from the gas-upwelling area (Fig. 1). The 60-mm-diameter cores were extracted during cruise MSM78 (Karstens et al., 2019) using the remotely operated Rock Drill 2 system (RD2, British Geological Survey). The RD2 drilled 35 m deep through unconsolidated glaciomarine sediments and tills with at least 24% recovery. The patchy, low-rate recovery is attributed to the presence of intervals dominated by low-cohesion sandy sediments, whose structure did not sustain the drilling stress and which therefore fell out of the core liner during recovery (Karstens et al., 2019).

#### 3.1. Physical parameters from core logging

The sediment cores were logged at intervals of 1 cm using the MSCL (Geotek, 2016) at the BOSCORF laboratory of the National Oceanography Centre Southampton. Bulk density is measured using the gamma ray attenuation method (Evans, 1965) and a 7.6 cm-wide sensor. Porosities are estimated from the measured bulk density  $D_b$  using  $\phi = (D_b - D_g) / (D_f - D_g)$  with grain density  $D_g = 2.65 \text{ g/cm}^3$  and fluid density  $D_f = 1 \text{ g/cm}^3$  (Geotek, 2016).

Resistivity is measured by inducing a high-frequency time-varying electric field in the sample. A receiving coil offset by 2 cm detects the magnetic field induced in the sample which is directly proportional to the material conductivity (McNeil, 1980). In order to improve the signal-to-noise ratio, variations attributed to the local environment detected by an identical set of coils operating in air are removed (Jackson et al., 2006).

The MSCL data show an increase in resistivity with depth and a decrease in porosity (Fig. 6a). For some sections porosities vary over a range of 0.15 and resistivities over a range of 0.4  $\Omega\text{m}$ , probably due to small sections of unconsolidated material losing integrity and water content after recovery and during core storage.

#### 3.2. Calibration of Archie's parameters

The MSCL data of the unconsolidated sections follow a distinct trend when plotting formation factor (bulk vs fluid resistivity ratio) against porosity (Fig. 6b) amid the presence of outliers. The fluid resistivity is decreased from 0.278  $\Omega\text{m}$  measured with DASI's CTD 20 m above the seabed to 0.2  $\Omega\text{m}$  in the lab due to the temperature increase to 20 °C (McDougall and Barker, 2011; Riedel et al., 2006). Archie's relationship (Eq. (2)) is fit to the data points using a non-linear optimisation technique (adaptive downhill-simplex simulated annealing, Dosso et al., 2001), but other algorithms work as well (such as bootstrapping, Riedel et al., 2020). To explore the ambiguity given the noisiness of the data, we sample interchangeable combinations of  $a$  and  $m$  and accept the models within the standard deviation of the logging data (similar to Sava and Hardage, 2006; Schwalenberg et al., 2020). The relationship  $m = -1.19a + 2.63 \pm 0.04$  is inferred (Fig. 6b inlay), with optimal values of  $a$  between about 0.8 and 1.1 and  $m$  between 1.3 and 1.7. These relatively small values of  $a$  and  $m$  indicate that the sediment is unconsolidated and the pore space is well connected (Pearson et al., 1983). Archie's law was extended to incorporate clay using the Waxman–Smits model (e.g., Mavko et al., 1998; Sahoo et al., 2018), which includes further

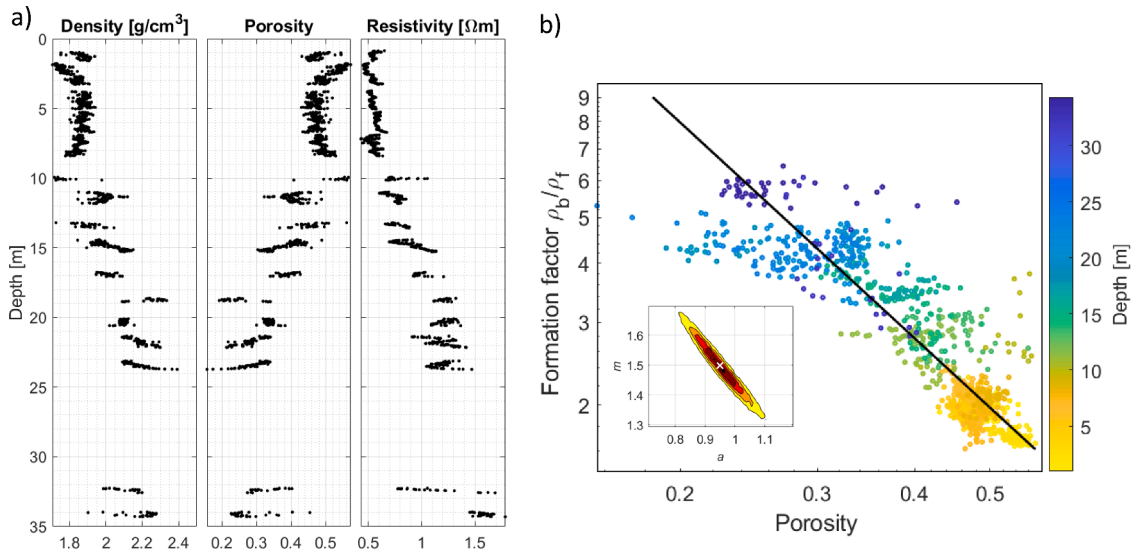


Fig. 6. (a) Density, density-derived porosity and electrical resistivity from MSCL measurements on sediment cores acquired by drill rig RD2 at a reference site 6 km North East of the pockmark (Karstens et al., 2019); (b) Formation factor (bulk vs. fluid resistivity ratio) versus porosity from MSCL measurements colour-coded by depth, and Archie’s empirical relationship (black line) with best-fit Archie parameters  $a = 0.95$  and  $m = 1.5$  (white cross in probability density of  $a$  and  $m$ , inset).

unknowns such as the concentration of clay exchange cations. Analysis of log-scale data in the laboratory shows that there is some benefit from incorporating the clay extension (Falcon-Suarez et al., 2021). However, for our calibration we averaged Archie’s parameters over the depth section with variable clay content. The resistivity models are also averaging over a large volume, and in this case Archie’s relationship

seems sufficient given the lack of resolution and the goodness of fit that can be achieved (Fig. 6).

Archie’s relationship can be extended to estimate the gas saturations  $S_g = 1 - S$  in partially saturated sediments with fluid saturation

$$S = \sqrt[n]{a\phi^{-m}\frac{\rho_f}{\rho_b}} \tag{3}$$

where  $n$  is the saturation coefficient, which may depend on saturation and reach up to 2.5 (Cook and Waite, 2018; Pearson et al., 1983). Including seismic constraints and resistivities for four layers from the optimal resistivity models, we build synthetic models with a 20–40 m-thick gas pocket at 40 mbsf beneath the pockmark. The background resistivity for the synthetic models at the gas pocket depth is 1.2  $\Omega\text{m}$ . To relate resistivity to saturation and porosity we use best fit Archie’s parameters  $a = 0.95$  and  $m = 1.5$ . The resistivity does not increase much with a few percent of free gas (Fig. 7). For example, 10% of gas only causes an increase from 1.2 to about 1.5  $\Omega\text{m}$ . For larger saturations the saturation exponent becomes more relevant so that, for this case, saturations between 40% and 50% may cause resistivities from 2.6 to 6.5  $\Omega\text{m}$ .

### 3.3. Porosity estimation

The resistivity is sampled by generating random samples from a Gaussian distribution using the mean and standard deviation of the inferred resistivity profiles (Fig. 5b). Background porosities are estimated using Archie’s relationship (Eq. (2)) and decrease with depth from about  $50 \pm 10\%$  at the seafloor to  $25 \pm 3\%$  at 150 mbsf (Fig. 8).

The resistivity-derived porosities are compared to porosities estimated assuming a sediment compaction vs. effective stress relationship  $\phi = \phi_0 e^{-\beta\sigma'}$ , where the compressibility of saturated sediments is represented by the parameter  $\beta$ , which ranges between  $2 \times 10^{-6} \text{ Pa}^{-1}$  for plastic clay to  $6.9 \times 10^{-8} \text{ Pa}^{-1}$  for dense clay, and between  $10^{-7} \text{ Pa}^{-1}$  for loose and  $1.3 \times 10^{-8} \text{ Pa}^{-1}$  for dense sand (e.g., Marin-Moreno et al., 2013). Here, we use average values of  $2.5\text{--}6.5 \times 10^{-7} \text{ Pa}^{-1}$  considering the high clay content of the sediment at the Scanner Pockmark (dashed lines Fig. 8). The effective stress  $\sigma'$  is defined as the lithostatic pressure minus the pore water pressure, which under hydrostatic conditions is expressed as  $\sigma' = g \cdot (D_b - D_f) \cdot \Delta z$ , where  $\Delta z$  is the depth below the seafloor and  $g$  is the acceleration due to gravity. Matching porosity results

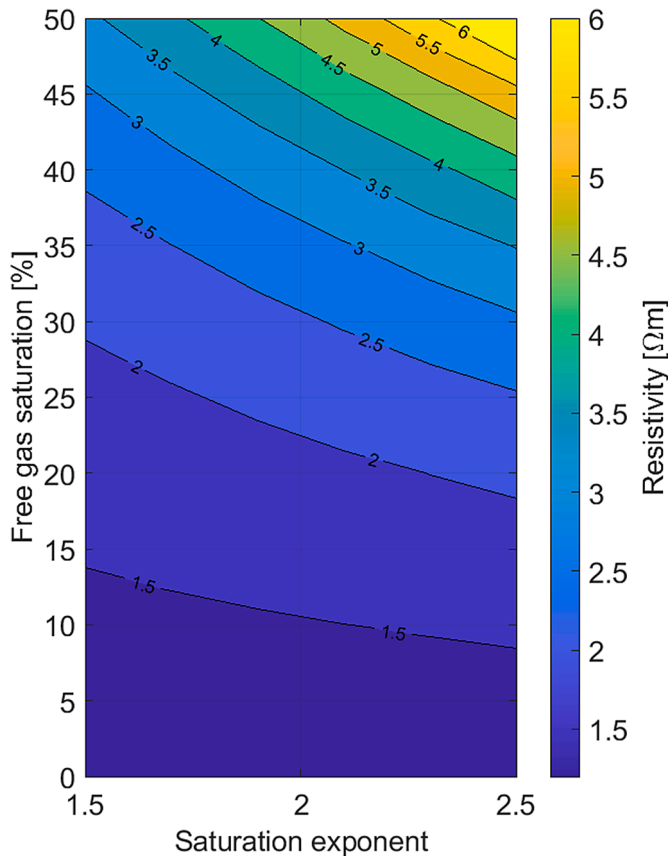
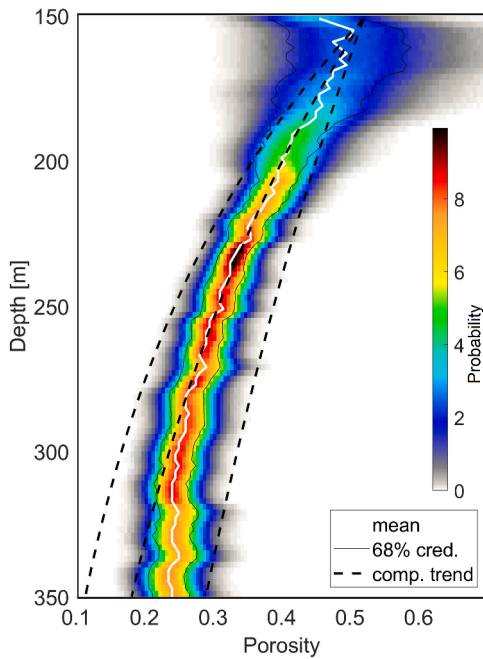


Fig. 7. Resistivity from free gas saturation against saturation exponent  $n$  from Archie’s relationship using 30% porosity, 0.278  $\Omega\text{m}$  pore water resistivity,  $a = 0.95$ , and  $m = 1.5$ .



**Fig. 8.** Probability (in per cent for each interval at each depth section) for porosity against depth from background electrical resistivity models (Fig. 5 b) with mean value (white line) and 68% confidence intervals (black lines). Porosities from compaction with depth are shown in dashed lines with compressibility  $\beta$  varying between  $2.5 \times 10^{-7} \text{ Pa}^{-1}$  and  $6.5 \times 10^{-7} \text{ Pa}^{-1}$ .

from this relationship and estimates from resistivities suggest that, for the purposes of this study, the sediments between the analysed depths can be represented as a homogeneous medium with porosity changes with depth mainly controlled by mechanical compaction. The deviation from the trend at depths greater 150 mbsf could be related to a loss of CSEM data sensitivity for the short offsets used and a resulting flat resistivity trend.

#### 4. Seismic and electromagnetic data joint interpretation

##### 4.1. CSEM inversion results using seismic constraints

The CSEM inversion algorithm is regularised with the roughness term in Eq. (1), promoting a resistivity model with little contrasts. A gas pocket, however, will likely cause a resistivity jump at its top. The inherent ambiguity of CSEM data means that models with either a gradual or a sharp resistivity increase can explain the observed data. Including a penalty cut in the inversion (Key, 2016) that allows for a roughness increase at that boundary will therefore result in a more geologically reliable result. The geological boundary can be extracted from seismic reflection data because seismic impedance also changes at the gas pocket and causes a bright phase-reversed reflection (e.g., Gehrman et al., 2019). Inversions including a penalty cut at the bright spot at about 40 mbsf result in a resistivity contrast (shown for profiles P5 in Fig. 9 and P11 in Fig. 10, and for four profiles across the pockmark on Fig. 11).

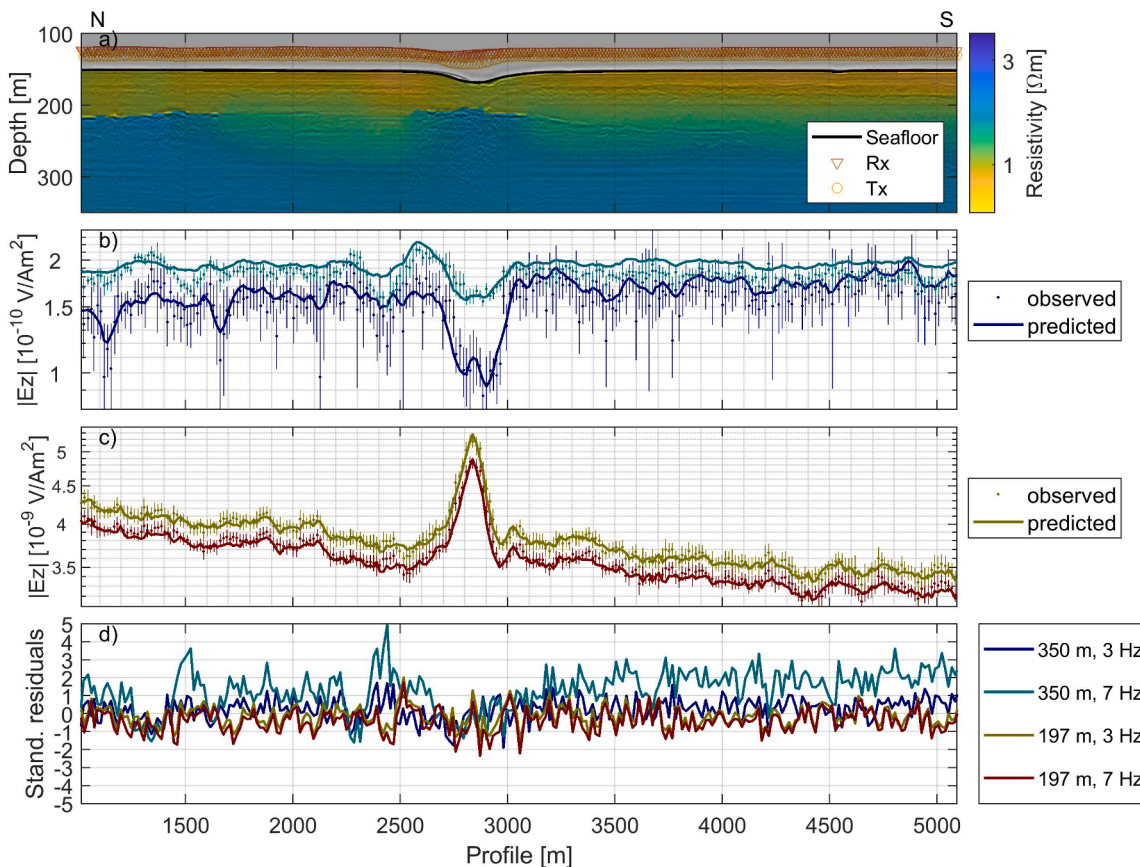


**Fig. 9.** Resistivity model (a) and vertical electric field amplitudes (b–c) for CSEM profile P5 with seismic constraints (at high reflectivity of seismic section for the horizon above the MIS6 deposit, dashed pink line shown in Fig. 2). The amplitudes for the vertical electric field  $E_z$  are shown on panel b for the furthest Vulcan and c for the closest Vulcan, for observed (dots with error bars) and predicted data (solid lines). Standardised residuals for both receivers are shown on panel d.  $E_z$  is sensitive to the tilt of the instrument, which explains the amplitude peaks and troughs when the instrument height is adjusted (example shown in supplementary material).



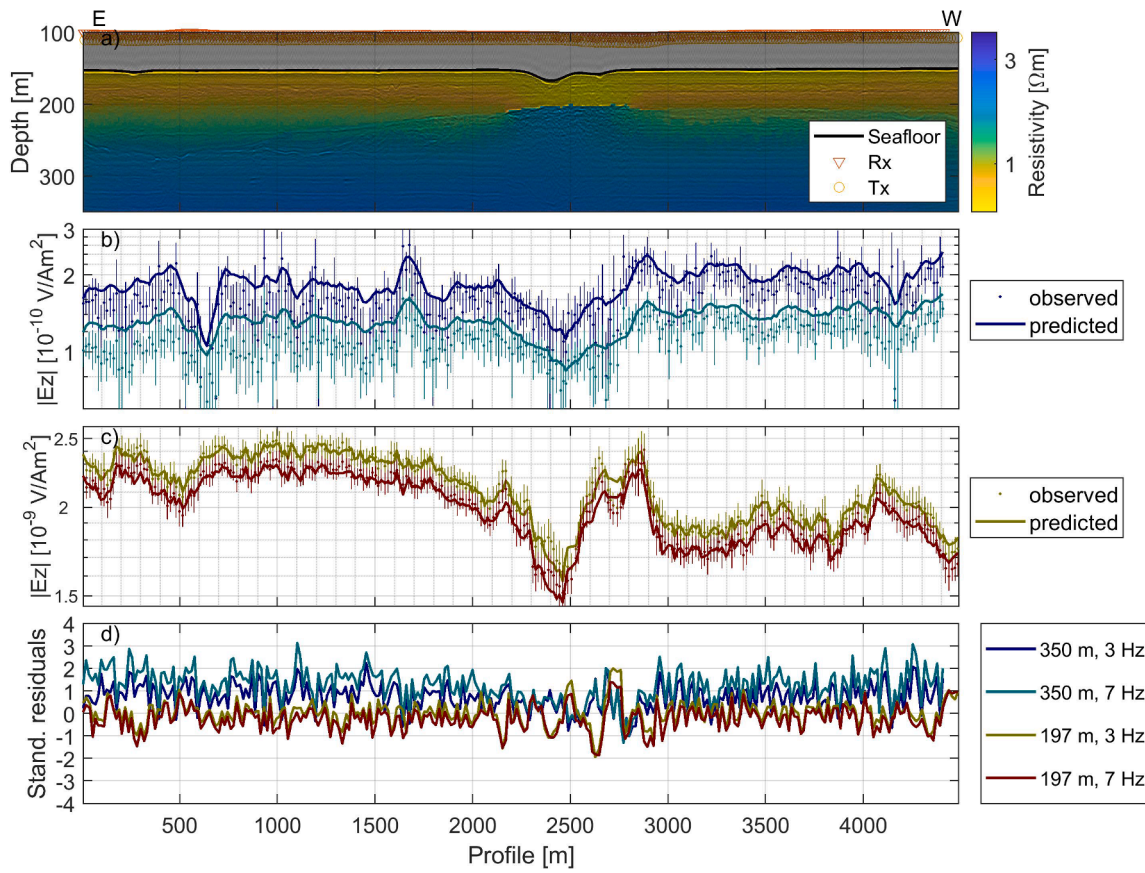


**Fig. 10.** Resistivity model (a) and vertical electric field amplitudes (b–c) for CSEM profile P11 (perpendicular to P5) with seismic constraints (at high reflectivity of seismic section for the horizon above the MIS6 deposit, dashed pink line shown in Fig. 2). The amplitudes for the vertical electric field  $E_z$  are shown on panel b for the furthest Vulcan and c for the closest Vulcan, for observed (dots with error bars) and predicted data (solid lines). Standardised residuals for both receivers are shown on panel d.

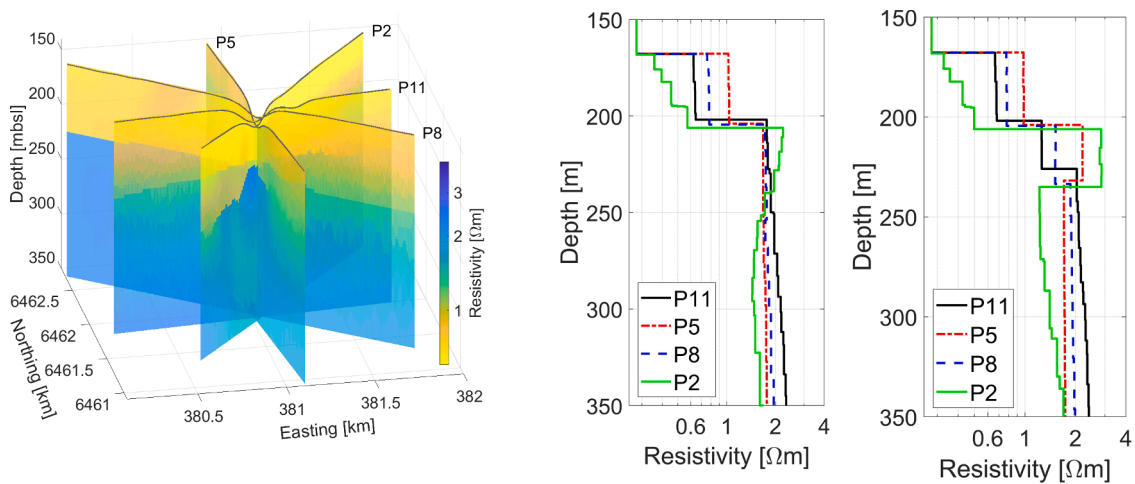


**Fig. 11.** Left: Resistivity models for four profiles across the Scanner Pockmark where the top of the gas pocket is constrained from seismic data; Middle: Vertical resistivity profiles from the centre of the pockmark; Right: Vertical resistivity profiles from the centre of the pockmark from inversions where the bottom of the gas pocket is also constrained.

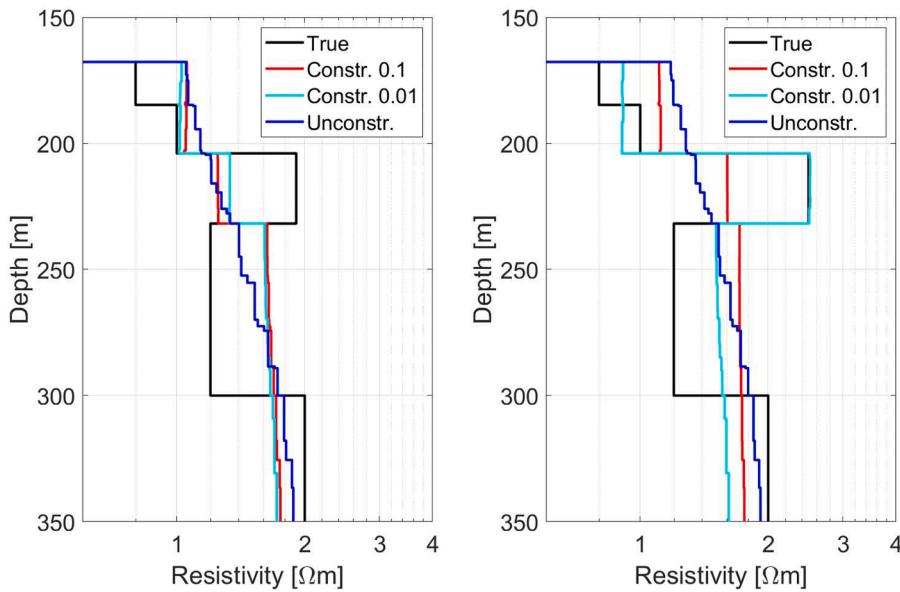


**Fig. 12.** Vertical resistivity depth profiles at the centre of the pockmark for synthetic data inversion for the true model (black line) with realistic data error, for an unconstrained model (blue line) and including seismic constraints. The smoothness regularisation is reduced above and below the gas pocket at about 210 mbsl and about 235 mbsl using a multiplier of 0.1 (red line) and 0.01 (turquoise line) which is applied to the model roughness operator (eq. 34 in Key, 2016). Left: Result for small increase in resistivity in gas pocket; Right: Result for larger increase in resistivity and higher free gas concentration. (For interpretation of the references to colour in this figure legend, the reader is referred to the web version of this article.)

#### 4.2. Free gas estimation

To investigate further how much free gas is required to cause a significant anomaly above the data error, we invert synthetic data with realistic errors from profile P5 (Fig. 9). The true model includes a ~30-m thick gas pocket (Fig. 12) whose top and bottom are constrained in the inversion. The resistivity for the gas pocket is estimated using Eq. (3) and  $a=0.95$ ,  $m=1.5$ , and  $1.5 < n < 2.5$ . Therefore, 18–28% free gas causes a resistivity of 1.9  $\Omega\text{m}$  compared to 1.2  $\Omega\text{m}$  without gas. The inferred models (reaching a misfit of  $\sim 1$ ) do not incorporate a gas pocket because the data anomaly is below the data error, and the resistivity increases smoothly instead. For a resistivity of 2.5  $\Omega\text{m}$ , however, the final model incorporates the resistive gas pocket. A resistivity of 2.5  $\Omega\text{m}$  corresponds to a range of 25–40% free gas because of the uncertainty in the saturation exponent  $n$  (Fig. 7). We conclude that at least  $33 \pm 8\%$  gas saturation is required to be resolved. Including a constraint on the bottom of the gas occurrence in the real data inversion leads to an abrupt decrease in resistivity for P5 and P2 (Fig. 11 right), but not for P8 and P11, perhaps because the amount of gas is at the limit of the data sensitivity or because its lower boundary is not sharp. It is less clear from seismic data that there is a sharp lower boundary. The following interpretation is therefore done from inversion results where only the top of the gas pocket is constrained.

Resistivity models inferred for profiles P2, P5, P8 and P11 using the bright spot as a constraint (Fig. 11) result in free gas estimations of up to 34% (Fig. 13). Absolute uncertainty estimates (e.g., Malinverno et al., 2008) are based on adding the uncertainty for each parameter in eq. 3 (by taking the respective derivative and multiplying it with the standard deviation estimate) and reach up to 14%. The main contributors to the uncertainty are the standard deviation of the inferred resistivity (Fig. 5 b) and porosity (Fig. 8). The thickness of the free gas saturated layer varies between 30 to 40 m beneath the pockmark when considering only gas estimations above their uncertainty. Along profile P8 towards the NWW the thickness may reach up to 50 m.

## 5. Discussion

We present an estimate of porosity from towed CSEM data down to 200 mbsf. CSEM data for all profiles can be explained with a gradual resistivity increase with depth (Fig. 5). Resistivities increase from 0.6–1  $\Omega\text{m}$ , typical for unconsolidated marine sediments, at the surface to 2–2.6  $\Omega\text{m}$  at 200 mbsf. The resistivity increase flattens out below 150

mbsf, which could also be explained by reaching the penetration limit controlled by the maximum dipole-dipole offset of only about 300 m. When the data sensitivity is reduced, the roughness term in eq. 1 is weighted more strongly and penalises resistivity change.

Porosity estimation from resistivity profiles requires calibration of Archie's parameters using logging data (e.g., Riedel et al., 2006). We use MSCL data from cores extracted at a reference site about 6 km from the Scanner Pockmark. The cores do not show degassing structures, but are incomplete having lost sandy sections and losing integrity at the borders of intact sediment sections, which likely causes the few outliers in the data (Fig. 6). The resistivity-porosity trend (Fig. 6b), however, is evident and can be fit with Archie's relationship using best fit Archie's parameters  $a = 0.95$  and  $m = 1.5$ , which are reasonable values for unconsolidated sediments with well-connected pore space (Hearst et al., 2000). Porosity decreases with depth from  $50 \pm 10\%$  at the seafloor to  $25 \pm 3\%$  at 150 mbsf and matches values from a porosity vs. effective stress relationship well, suggesting that low frequency porosity changes throughout the sediments in the first 150 m are mainly controlled by mechanical compaction. The best fit is reached for a value for  $\beta = 4.5 \times 10^{-7} \text{ Pa}^{-1}$  indicating that the compressibility of the sediment is larger than for loose sand due to the high content of fine-grained components (e.g. Marin-Moreno et al., 2013).

Porosities from this mechanical compaction relationship start deviating from the resistivity derived porosities below  $\sim 150$  mbsf likely due to the reduction of CSEM data sensitivity. Resistivities would need to increase further with depth to follow the compaction trend. We expect that when we introduce the data from the ocean bottom instruments we will gain more sensitivity at depths  $>150$  mbsf. The towed data, however, are more sensitive to the gas pocket at 40 mbsf, due to the shorter offsets.

Inferred resistivity models are ambiguous and depend on the choice of inversion algorithm (e.g., Constable et al., 2015). Ambiguity can be addressed using prior constraints, for example, resistivity limits from logging data (e.g., Schwalenberg et al., 2020), or structural constraints from seismic reflection data (e.g., Gehrman et al., 2019). We use collocated seismic reflection data from the same cruise MSM63 (Berndt et al., 2017) with a vertical resolution of about 2.5 m. Seismic reflection data in this case can constrain the resistivity model by adding information about the top of the gas bearing layer, which is a contrast in resistivity and in seismic velocity alike. In synthetic tests, strongly reducing the smoothness regularisation at this boundary causes the inversion to find an optimal model close to the true model (Fig. 12).

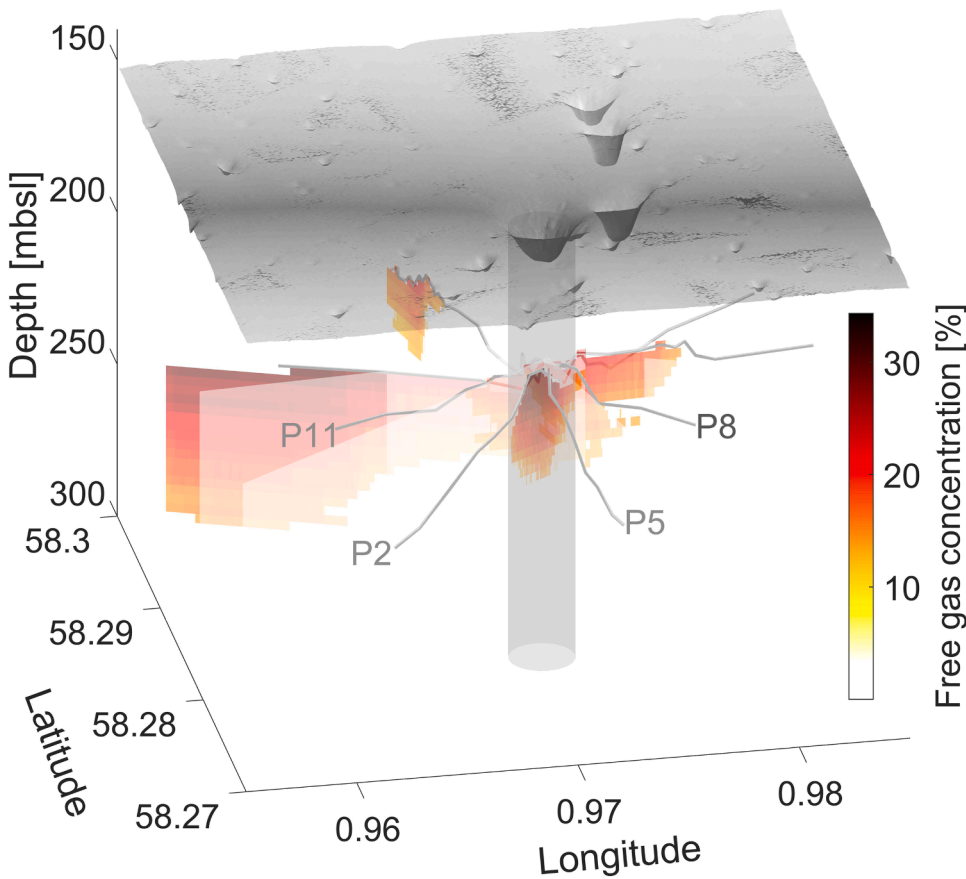


**Fig. 13.** Free gas estimates, shown only when the free gas estimates from CSEM data are above their uncertainty based on uncertainty assumptions made for various parameters using Archie’s relationship, for profiles P2, P5, P8 and P11 across the Scanner Pockmark using resistivity models, optimal Archie parameters  $\alpha=0.95$ ,  $m=1.5$ , and  $n=2$ . Bathymetry and approximate location of vertical fluid conduit are shown in grey. Grey lines mark the top of the gas bearing layer in glacial tills beneath the Coal Pit Formation and above the Aberdeen Ground Formation.

To study the sensitivity of the CSEM data to a shallow gas pocket, two synthetic studies were performed. First, forward modelling for a model with and without a shallow gas pocket was used to estimate the optimal frequency range of the vertical electric field amplitude data. The result (Fig. 4) suggests that frequencies from 1 to 7 Hz have the most diverse information content about the gas pocket, while higher frequencies, although strongly present in the data, seem to have redundant information. Second, synthetic data inversions for a model containing a

shallow gas pocket with varying gas content (Fig. 12) suggest that  $\sim 33 \pm 8\%$  of gas are required to cause a data anomaly larger than the data error. For CSEM the product of resistivity and layer thickness can be better resolved than each parameter individually (Edwards, 1997), so that different combinations of resistivity and thickness may be equivalent. A model with a gas pocket will be interpreted as a gradual change when not using seismic constraints (Fig. 12) because the inversion algorithm minimises the roughness term as well as the data fit (Eq. (1)).

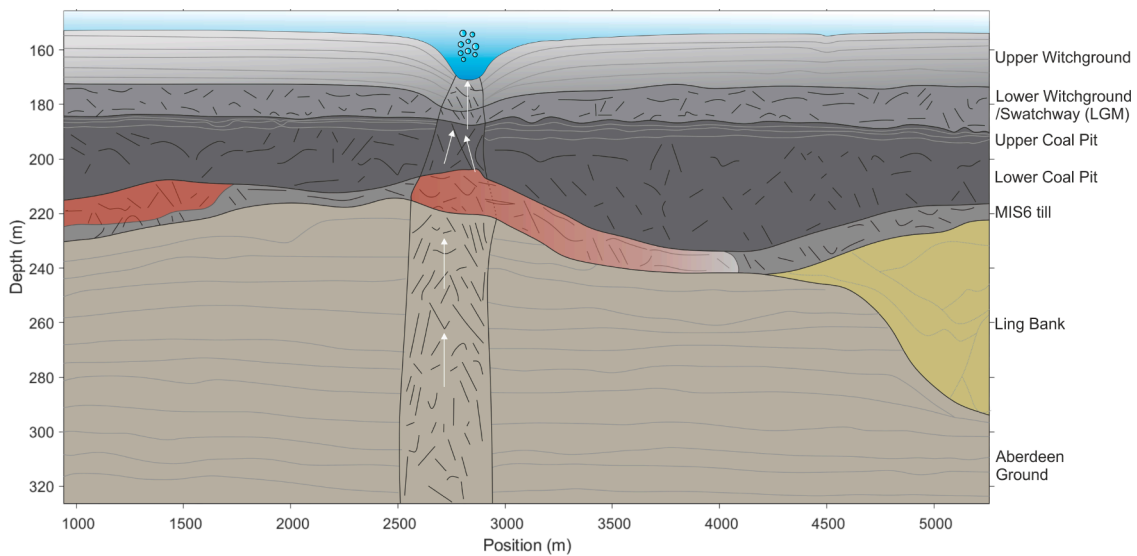


**Fig. 14.** Sketch of gas accumulations (red) in the glacial till layer (MIS6) between the clay-dominated Aberdeen Ground and Coal Pit Formations. The gas migrates (white arrows) vertically from deeper sources through the fluid pathway (seismic chimney, black vertical lines), causing active venting at the pockmark. (For interpretation of the references to colour in this figure legend, the reader is referred to the web version of this article.)

The data errors for the towed, vertical electric field amplitude data were estimated with a 2D perturbation study (Gehrman et al., 2019b) to encompass navigation uncertainties. Data errors are relatively large for the furthest Vulcan (about 10%) and only a few percent for the closest Vulcan (Fig. 10). The data fit for the final resistivity models (Figs. 9 and 10 d) is therefore generally better for the closest Vulcan than for the furthest which exhibits slightly biased standardised residuals. For real data inversions, the data fit for all profiles is comparable, for example, perpendicular profiles P5 and P11 shown in Figs. 9 and 10, where the source was towed at different heights above the seabed (20 and 40 m respectively). The ambiguity for different constraints is evident. For example, including constraints from seismic data at the high amplitude reflection beneath the pockmark on profile P11 (Fig. 10) results in resistivities being lower for the sediment column above the reflector than next to the pockmark where resistivities increase gradually. Including a bottom constraint for the gas pocket leads to the inferred model to have a step-wise increase of resistivity with depth (Fig. 11 right), while the inversions for P2 and P5 converge to a model including a thin resistive layer. The observed ambiguity is increased by using only  $E_z$  amplitude data (uncertainty in phase data discussed in Appendix A), and also because the bottom of the gas bearing layer is not well constrained. Optimal models for all profiles agree well when including only the constraint for the top of the resistive layer (Fig. 11 left).

Gas saturation estimates (Fig. 13) from CSEM data suggest a 30–40 m thick gas pocket (for gas estimates larger than their uncertainty). The maximum thickness of the gas layer is estimated to be ~50 m along profile P8 towards the NWW. When the gas column reaches a thickness and a pressure high enough to overcome the capillary entry pressure the gas moves vertically through the clay dominated glacial tills of the Coal Pit and Swathway Formation and form pockmarks at the surface (Fig. 14). We expect the gas bearing layer to be a few 10s of metres thick based on the pressure required to fracture the cap rock or to overcome the capillary entry pressure (e.g., Zhang and Sanderson, 2002). Li et al. (2020) observed continuous gas venting with an estimated flux of  $1.6\text{--}2.7 \cdot 10^6$  kg/year. To support the continuous venting requires that the shallow reservoir is constantly fed from deeper sources. While evidence of active fracturing has not been observed in high-frequency datasets such as parasound data (Böttner et al., 2019), shear wave splitting and P-wave velocity anisotropy in the upper 40 mbsf below the pockmark (Bayrakci et al., 2020) suggest the presence of fractures.

Although gas saturation estimates from the inferred resistivity models using seismic constraints (Fig. 13) come with an absolute uncertainty of up to 14%, the fact that they reach up to 34% is a robust indicator for gas accumulating in the stratigraphic highs in the glacial tills just above the Aberdeen Ground Formation (Fig. 14). Combined seismic and CSEM data interpretation suggest that the gas pocket has an irregular shape reaching 500 m to 700 m in width on profiles P5, P2 and P11, but extending to the NWW on profile P8 along a stratigraphic high. Several profiles suggest the presence of free gas in the glacial tills without a pockmark directly above, indicating lateral movement of the gas within the tills.

## 6. Conclusions

The Scanner Pockmark area is abundant in two classes (class 1: large, class 2: small) of pockmarks. Class 1 pockmarks are possibly connected to deep vertical/subvertical fluid conduits that act as pathways for methane gas venting at the surface. Beneath a relatively impermeable sediment interval, the glaciomarine Coal Pit Formation, free gas accumulates forming a gas pocket before breaching occurs and the gas reaches the surface. Here, we show how towed controlled-source electromagnetic data can be used to estimate the background porosity and the free gas content. Both are estimated using Archie's relationship by calibrating Archie's parameters with core logging data. Inversion of

vertical electric field amplitude data from twelve profiles gives a background resistivity trend increasing from 0.6–1  $\Omega\text{m}$  at the surface to 1.9–2.4  $\Omega\text{m}$  at 150 mbsf. Considering the uncertainties of resistivity and Archie's parameters, porosity is estimated to decrease from about  $50 \pm 10\%$  at the seafloor to  $25 \pm 3\%$  at 150 mbsf, which matches porosity estimates from mechanical compaction of clay rich sediments.

Resistivity models constrained with structural information from seismic reflection data suggest a resistive area at about 40 mbsf at the pockmark that can be interpreted as a shallow gas pocket. A synthetic data study shows that at least  $33 \pm 8\%$  free gas is required to cause an anomaly in the CSEM data that is large enough to be inferred in the inversion. Gas concentrations are estimated to be at the resolution limit for all four profiles across the pockmark supporting gas accumulations 30–40 m thick with up to  $34 \pm 14\%$  free gas (Figs. 13 and 14) that act as an intermediate reservoir for the gas to migrate from greater depth to the surface and cause observed venting at the surface.

## CRediT authorship contribution statement

**Romina A.S. Gehrman:** Conceptualization, Methodology, Software, Validation, Formal analysis, Investigation, Data curation, Writing - original draft, Writing - review & editing, Visualization. **Giuseppe Provenzano:** Methodology, Software, Writing - original draft, Writing - review & editing, Visualization. **Christoph Böttner:** Investigation, Writing - original draft, Writing - review & editing, Visualization. **Héctor Marín-Moreno:** Methodology, Writing - review & editing. **Gaye Bayrakci:** Investigation, Writing - review & editing. **Yee Y. Tan:** Investigation, Writing - review & editing. **Naima K. Yilo:** Investigation, Writing - review & editing. **Axel T. Djanni:** Investigation, Writing - review & editing. **Karen A. Weitemeyer:** Writing - review & editing. **Timothy A. Minshull:** Conceptualization, Resources, Writing - review & editing, Supervision, Project administration, Funding acquisition. **Jonathan M. Bull:** Conceptualization, Resources, Writing - review & editing, Supervision, Project administration, Funding acquisition. **Jens Karstens:** Investigation, Writing - review & editing. **Christian Berndt:** Investigation, Resources, Supervision, Project administration, Funding acquisition.

## Declaration of Competing Interest

The authors declare that they have no known competing financial interests or personal relationships that could have appeared to influence the work reported in this paper.

## Acknowledgements

We would like to thank the MSM63 and MSM78 cruise crews and scientific parties, especially the Ocean Bottom Instrument Consortium team and Laurence North for CSEM instrumentation support, the GEOMAR seismic data acquisition and processing team, and the BGS Rock Drill 2 team. We thank the British Ocean Sediment Core Research Facility team, especially Millie Watts, for the core data and the helpful discussions. We are grateful to Steven Constable from Scripps Institution of Oceanography, USA, for advise and lending eight CSEM data loggers for the survey. CSEM processing and inversion input routines are based on scripts by David Myer and Kerry Key. We would like to thank Kerry Key for his advise regarding the phase inversion. We thank two anonymous reviewers for their constructive comments. This work was supported by the European Union's Horizon 2020 research and innovation program under grant agreement no. 654462 and NERC grant NE/N01610/1. We acknowledge the use of the IRIDIS High Performance Computing Facility, and associated support services at the University of Southampton, in the completion of this work. The CSEM and seismic data sets are available at Gehrman et al. (2020) and Böttner and Berndt (2019).

**Appendix A. Phase analysis**

The resistivity models shown in the main body of this paper are based on amplitude data only. The information of the phase lag between source and receiver, however, may contain additional information about the resistivity structure in the chimney (see forward models in Fig. A.15 equivalent to the amplitude models in Fig. 4c and d).

During the processing we apply a time correction to the data depending on the clock synchronisation before and after deployment of the GPS triggered source and the independent quartz clocks in the receiver units. Preliminary analyses have shown that the observed phase data do not match the predicted data, which can be caused by an additional time delay in the hardware or deviation in the navigation parameters that we have not accounted for. Similarly to the static shift in magnetotelluric inversion with MARE2DEM (Key, 2016) we invert for this time delay between the source and receiver timing within each iteration of the model update calculating the residuals of the observed and predicted phase  $\delta\phi = \phi_o - \phi_p$  and estimating the time delay as an average over all  $N$  frequencies with

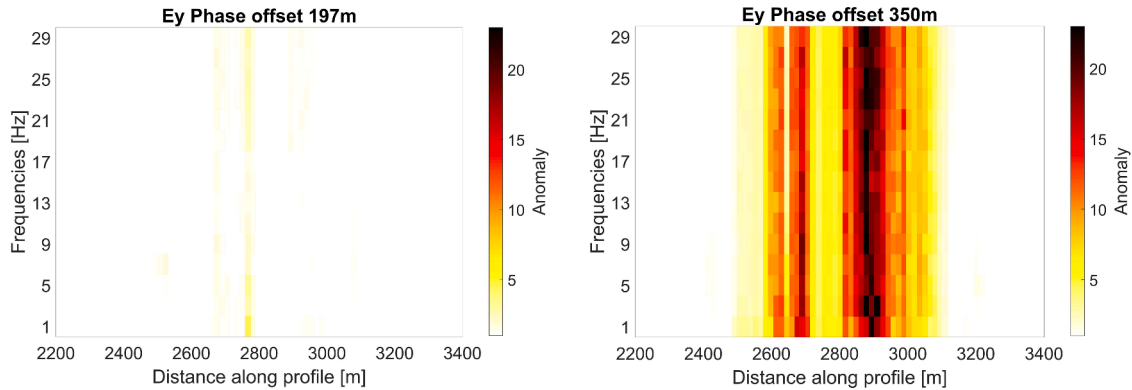


**Fig. A.15.** Data misfit for synthetic phase data for a synthetic model with and without a resistivity increase from 1.2  $\Omega\text{m}$  to 3.4  $\Omega\text{m}$  (corresponding to about 35 to 50% free gas depending on the saturation exponent, Fig. 7) at a gas pocket underneath the pockmark for 1 to 29 Hz.

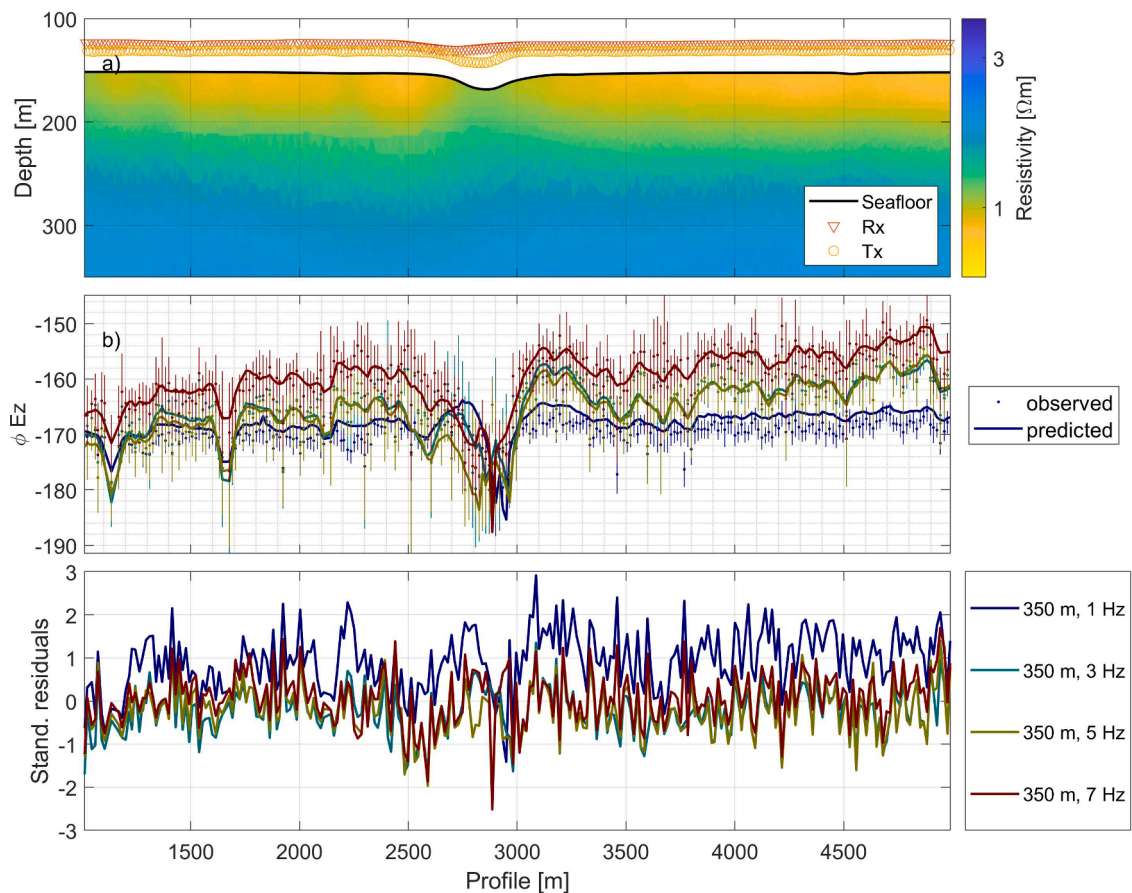


**Fig. A.16.** a) Profile P5 resistivity model for  $E_z$  amplitude and phase for the furthest Vulcan without seismic constraints; b) Observed and predicted phase data for 1 to 7 Hz; c) Standardised residuals for phase data (b).

$$dt = \frac{1}{N} \sum_{i=1}^N \frac{\delta\varphi_i}{2\pi f_i}, \quad (\text{A.1})$$

so that the new phase  $\varphi'_p = \varphi_p + 2\pi f dt$  is updated in every iteration and then used to calculate the data fit. The inversion generally runs slower when including the time delay as an additional parameter and the resistivity model is not as stable (for example, includes artefacts that cannot be explained geologically or do not match between intersecting profiles and seem to depend on the starting model) as without the time delay. Reasons for this may be that the update of the model and the time delay estimation are done in two different steps. The data fit is then calculated for the estimated time delay which may bias the weight of phase and amplitude in the update. The result of the time delay is, however, relatively steady in the ms range. To increase the stability of the result and the inversion time, the optimal model of the amplitude only inversions are chosen as the starting model. The inversions were run for profiles P2 to P8 and time delays for the closest receiver range between 13.9 and 24.4 ms and for the furthest receiver between 16.6 and 24.7 ms. The results indicate that the observed phase deviation is indeed caused by a time delay, but it is not clear if it is a receiver or source caused reason. For simplicity first tests were done for one time delay of 16.8 ms added to the transmitter clock for profile P5 for the furthest receiver (Fig. A.16). With the presented technique we can estimate a time delay and fit the phase. Further studies need to be done to estimate the accuracy that is achieved and if the additional analysis adds more information to the resistivity model.

## Supplementary material

Supplementary material associated with this article can be found, in the online version, at [10.1016/j.ijggc.2021.103343](https://doi.org/10.1016/j.ijggc.2021.103343)

## References

- Andrés, D., MacGregor, L., 2008. Controlled-source electromagnetic sounding in shallow water: Principles and applications. *Geophysics* 73 (1), F21–F32.
- Andresen, K.J., 2012. Fluid flow features in hydrocarbon plumbing systems: What do they tell us about the basin evolution? *Mar. Geol.* 332, 89–108.
- Archie, G.E., 1942. The electrical resistivity log as an aid in determining some reservoir characteristics. *Trans. Am. Inst. Min. Metall. Pet. Eng.* 146, 54–62.
- Arnts, W., Wensaas, L., Løseth, H., Hermanrud, C., 2007. Seismic modeling of gas chimneys. *Geophysics* 72 (5), SM251–SM259. <https://doi.org/10.1190/1.2749570>.
- Bayrakci, G., Minshull, T. A., Bull, J. M., Henstock, T. J., Provenzano, G., Birinci, H., Macdonald, C., Dunn, R., 2020. P-wave velocity anisotropy in an active methane venting pockmark: The Scanner Pockmark, northern North Sea. *EGU2020online*. 10.5194.
- Berndt, C., Elger, J., Böttner, C., Gehrman, R., Karstens, J., Muff, S., Pitcairn, B., Schramm, B., Lichtschlag, A., Völsch, A., 2017. RV MARIA S. MERIAN Fahrtbericht / Cruise Report MSM63 - PERMO, Southampton - Southampton (U.K.) 29.04.-25.05.2017. *GEOMAR Report N.Ser.* 037. 10.3289.
- Boait, F.C., White, N.J., Bickle, M.J., Chadwick, R.A., Neufeld, J.A., Huppert, H.E., 2012. Spatial and temporal evolution of injected CO<sub>2</sub> at the sleipner field, north sea. *J. Geophys. Res.* 117 (B3).
- Böttner, C., Berndt, C., 2019. 2D seismic, echosounder and multibeam data of the Witch Ground Basin (central North Sea) during Maria S. Merian cruise MSM63.
- Böttner, C., Berndt, C., Reinardy, B.T., Geersen, J., Karstens, J., Bull, J.M., Callow, B.J., Lichtschlag, A., Schmidt, M., Elger, J., Schramm, B., Haeckel, M., 2019. Pockmarks in the Witch Ground Basin, Central North Sea. *Geochem. Geophys. Geosyst.* 20 (4), 1698–1719. <https://doi.org/10.1029/2018GC008068>.
- Bünz, S., Mienert, J., Berndt, C., 2003. Geological controls on the Storegga gas-hydrate system of the mid-Norwegian continental margin. *Earth Planet. Sci. Lett.* 209 (3), 291–307. [https://doi.org/10.1016/S0012-821X\(03\)00097-9](https://doi.org/10.1016/S0012-821X(03)00097-9).
- Cartwright, J., Huuse, M., Aplin, A., 2007. Seal bypass systems. *Am. Assoc. Pet. Geol. Bull.* 91 (8), 1141–1166. <https://doi.org/10.1306/04090705181>.
- Chave, A.D., Cox, C.S., 1982. Controlled electromagnetic sources for measuring electrical conductivity beneath the oceans I. Forward problem and model study. *J. Geophys. Res.* 87 (B7), 5327–5338.
- Constable, S.C., 2010. Ten years of marine CSEM for hydrocarbon exploration. *Geophysics* 75 (5), 75A67–75A81.
- Constable, S.C., Kannberg, P.K., Weitemeyer, K., 2016. Vulcan: A deep-towed CSEM receiver. *Geochem. Geophys. Geosyst.* 17 (3), 1042–1064. <https://doi.org/10.1002/2015GC006174>.
- Constable, S., Orange, A., Key, K., 2015. And the geophysicist replied: Which model do you want? *Geophysics* 80 (3), E197–E212.
- Constable, S.C., Parker, R.L., Constable, C.G., 1987. Occam's inversion: A practical algorithm for generating smooth models from electromagnetic sounding data. *Geophysics* 52, 289–300.
- Cook, A.E., Waite, W.F., 2018. Archie's saturation exponent for natural gas hydrate in coarse-grained reservoirs. *J. Geophys. Res.* 123 (3), 2069–2089. <https://doi.org/10.1002/2017JB015138>.
- Dean, M., Tucker, O., 2017. A risk-based framework for Measurement, Monitoring and Verification (MMV) of the Goldeneye storage complex for the Peterhead CCS project, UK. *Int. J. Greenhouse Gas Control* 61, 1–15. <https://doi.org/10.1016/j.ijggc.2017.03.014>.
- Dosso, S.E., Wilmut, M.J., Lapinski, A.-L.S., 2001. An adaptive-hybrid algorithm for geoaoustic inversion. *Ocean. Eng. IEEE J.* 26 (3), 324–336.
- Edwards, R.N., 1997. On the resource evaluation of marine gas hydrate deposits using sea-floor transient electric dipole-dipole methods. *Geophysics* 62 (1), 63–74.
- Edwards, R.N., 2005. Marine controlled source electromagnetics: Principles, methodologies, future commercial applications. *Surveys in Geophysics*, 26. Springer, Berlin, Heidelberg, New York, pp. 675–700.
- Evans, H., 1965. Grape - a device for continuous determination of material density and porosity. *Proceedings of 6th Annual SPWLA Logging Symposium*. Dallas, TX, 2, pp. B1–B25.
- Falcon-Suarez, I.H., Lichtschlag, A., Marin-Moreno, H., Papageorgiou, G., Sahoo, S.K., Roche, B., Callow, B., Gehrman, R.A.S., Chapman, M., North, L., 2021. Core-scale geophysical and hydromechanical analysis of seabed sediments affected by CO<sub>2</sub> venting. *Int. J. Greenhouse Gas Control* 108, 103332.
- Gafeira, J., Long, D., 2015. Geological investigation of pockmarks in the Scanner Pockmark SCI area. *JNCC Rep.* 570, 1–88.
- Gehrman, R.A.S., Haroon, A., Morton, M., Djanni, A.T., Minshull, T.A., 2019. Seafloor massive sulphide exploration using deep-towed controlled source electromagnetics: navigational uncertainties. *Geophys. J. Int.* 220 (2), 1215–1227. <https://doi.org/10.1093/gji/ggz513>.
- Gehrman, R. A. S., Minshull, T. A., Yilo, N. K., Berndt, C., 2020. Ocean Bottom and deep-towed controlled source electric field data during cruise MSM63 on May 3rd to 5th 2017 across Scanner Pockmark, UK North Sea.
- Geotek, 2016. Multi-Sensor Core Logger - Manual.
- Gehrman, R.A., Schnabel, C., Engels, M., Schnabel, M., Schwalenberg, K., 2019. Combined interpretation of marine controlled source electromagnetic and reflection seismic data in the German North Sea: A case study. *Geophys. J. Int.* 216 (1), 218–230.
- Goswami, B.K., Weitemeyer, K.A., Bünz, S., Minshull, T.A., Westbrook, G.K., Ker, S., Sinha, M.C., 2017. Variations in pockmark composition at the Vestnesa Ridge: Insights from marine controlled source electromagnetic and seismic data. *Geochem. Geophys. Geosyst.* 18 (3), 1111–1125.
- Goswami, B.K., Weitemeyer, K.A., Minshull, T.A., Sinha, M.C., Westbrook, G.K., Chabert, A., Henstock, T.J., Ker, S., 2015. A joint electromagnetic and seismic study of an active pockmark within the hydrate stability field at the Vestnesa Ridge, West Svalbard margin. *J. Geophys. Res.* 120 (10), 6797–6822.
- Gustafson, C., Key, K., Evans, R.L., 2019. Aquifer systems extending far offshore on the US Atlantic margin. *Sci. Rep.* 9 (1), 1–10.
- Haroon, A., Lippert, K., Mogilatov, V., Tezkan, B., 2018. First application of the marine differential electric dipole for groundwater investigations: A case study from Bat Yam, Israel. *Geophysics* 83 (2), B59–B76. <https://doi.org/10.1190/geo2017-0162.1>.
- Hearst, J.R., Nelson, P.H., Paillet, F.L., 2000. *Well Logging for Physical Properties*, second ed. John Wiley, Hoboken, N.J.
- Hovland, M., Sommerville, J.H., 1985. Characteristics of two natural gas seepages in the North Sea. *Mar. Pet. Geol.* 2 (4), 319–326. [https://doi.org/10.1016/0264-8172\(85\)90027-3](https://doi.org/10.1016/0264-8172(85)90027-3).
- Jackson, P.D., Lovell, M.A., Roberts, J.A., Schultheiss, P.J., Gunn, D., Flint, R.C., Wood, A., Holmes, R., Frederichs, T., 2006. *Rapid Non-Contacting Resistivity Logging of core*, 267. Geological Society London, Special Publication, pp. 209–217.
- Judd, A.G., Long, D., Sankey, M., 1994. Pockmark formation and activity, UK block 15/25, North Sea. *Bull. Geol. Soc. Den.* 41 (1), 34–49.
- Kallweit, R., Wood, L., 1982. The limits of resolution of zero-phase wavelets. *Geophysics* 47, 1035–1046.
- Kannberg, P.K., Constable, S., 2020. Characterization and quantification of gas hydrates in the California borderlands. *Geophys. Res. Lett.* 47 (6) <https://doi.org/10.1029/2019GL084703>.
- Karstens, J., Böttner, C., Edwards, M., Falcon-Suarez, I., Flohr, A., James, R., Lichtschlag, A., Maicher, D., Pheasant, I., Roche, B., Schramm, B., Wilson, M., 2019. RV MARIA S. MERIAN Fahrtbericht / Cruise Report MSM78 - PERMO 2, Edinburgh - Edinburgh (U.K.) 16.10.-25.10.2018. *GEOMAR Report N.Ser.* 048. 10.3289/GEOMAR\_REP\_NS\_48\_2019.
- Karstens, J., Berndt, C., 2015. Seismic chimneys in the Southern Viking Graben - Implications for palaeo fluid migration and overpressure evolution. *Earth Planet. Sci. Lett.* 412, 88–100.

- Key, K., 2016. MARE2DEM: a 2-D inversion code for controlled-source electromagnetic and magnetotelluric data. *Geophys. J. Int.* 207 (1), 571–588. <https://doi.org/10.1093/gji/ggw290>.
- Li, J., Roche, B., Bull, J.M., White, P.R., Leighton, T.G., Provenzano, G., Dewar, M., Henstock, T.J., 2020. Broadband acoustic inversion for gas flux quantification-application to a methane plume at scanner pockmark, central north sea. *J. Geophys. Res.* 125 (9) <https://doi.org/10.1029/2020JC016360>.e2020JC016360
- Løseth, H., Gading, M., Wensaas, L., 2009. Hydrocarbon leakage interpreted on seismic data. *Mar. Pet. Geol.* 26 (7), 1304–1319. <https://doi.org/10.1016/j.marpetgeo.2008.09.008>.
- MacGregor, L.M., Andreis, D., Tomlinson, J., Barker, N., 2006. Controlled-source electromagnetic imaging on the Nuggets-1 reservoir. *Leading Edge* 25 (8), 984–992.
- Malinverno, A., Kastner, M., Torres, M.E., Wortmann, U.G., 2008. Gas hydrate occurrence from pore water chlorinity and downhole logs in a transect across the Cascadia margin (integrated ocean drilling program expedition 311). *J. Geophys. Res.* 113 (B08103).
- Mavko, G., Mukerji, T., Dvorkin, J., 1998. *The Rock Physics Handbook*. Cambridge University Press.
- Marin-Moreno, H., Minshull, T.A., Edwards, R.A., 2013. A disequilibrium compaction model constrained by seismic data and application to overpressure generation in the Eastern Black Sea Basin. *Basin Res.* 25 (3), 331–347. <https://doi.org/10.1111/bre.12001>.
- McNeil, J., 1980. Electromagnetic terrain conductivity measurement at low induction numbers. Technical Note TN-6, GEONICS Limited, Ontario, Canada.
- McDougall, T.J., Barker, P.M., 2011. Getting started with TEOS-10 and the Gibbs Seawater (GSW) oceanographic toolbox. *SCOR/IAPSO WG 127*, 1–28.
- Micallef, A., Person, M., Haroon, A., Weymer, B.A., Jegen, M., Schwalenberg, K., Faghih, Z., Duan, S., Cohen, D., Mountjoy, J.J., et al., 2020. 3D characterisation and quantification of an offshore freshened groundwater system in the Canterbury Bight. *Nat. Commun.* 11 (1), 1–15.
- Minshull, T., Sinha, M., Peirce, C., 2005. Multi-disciplinary, sub-seabed geophysical imaging - a new pool of 28 seafloor instruments in use by the United Kingdom ocean bottom instrumentation consortium. *Sea Technol.* 46 (10), 27–31.
- Morten, J.P., Bjørke, A., 2020. Imaging and Quantifying CO2 Containment Storage Loss Using 3D CSEM. 82nd EAGE Annual Conference & Exhibition, 2020. European Association of Geoscientists & Engineers, pp. 1–5.
- Myer, D., Constable, S., Key, K., 2011. Broad-band waveforms and robust processing for marine CSEM surveys. *Geophys. J. Int.* 184, 689–698.
- Naif, S., Key, K., Constable, S., Evans, R.L., 2015. Water-rich bending faults at the Middle America Trench. *Geochem. Geophys. Geosyst.* 16 (8), 2582–2597. <https://doi.org/10.1002/2015GC005927>.
- Park, J., Sauvin, G., Vöge, M., 2017. 2.5D inversion and joint interpretation of CSEM data at sleipner CO2 storage. *Energy Procedia* 114, 3989–3996. <https://doi.org/10.1016/j.egypro.2017.03.1531>. 13th International Conference on Greenhouse Gas Control Technologies, GHGT-13, 14–18 November 2016, Lausanne, Switzerland
- Peacock, K., Treitel, S., 1969. Predictive deconvolution - theory and practice. *Geophysics* 34, 155–169.
- Pearson, C.F., Halleck, P.M., McGuire, P.L., Hermes, R., Mathews, M., 1983. Natural gas hydrate deposits: A review of in situ properties. *J. Phys. Chem.* 87, 4180–4185.
- Reinardy, B.T., Hjelstuen, B.O., Sejrup, H.P., Augedal, H., Jørstad, A., 2017. Late pliocene-pleistocene environments and glacial history of the Northern North Sea. *Quat. Sci. Rev.* 158, 107–126.
- Riedel, M., Freudenthal, T., Bergenthal, M., Haeckel, M., Wallmann, K., Spangenberg, E., Bialas, J., Bohrmann, G., 2020. Physical properties and core-log seismic integration from drilling at the Danube deep-sea fan, Black Sea. *Mar. Pet. Geol.* 114, 104192. <https://doi.org/10.1016/j.marpetgeo.2019.104192>.
- Riedel, M., Long, P., Liu, C., Schultheiss, P., Collett, T., ODP Leg 204 Shipboard Scientific Party, 2006. Physical properties of near surface sediments at southern hydrate ridge: results from ODP leg 204. In Tréhu, A.M., Bohrmann, G., Torres, M.E., and Colwell, F.S. (Eds.), *Proceedings of the Ocean Drilling Program, Scientific Results*. 204: College Station, TX (Ocean Drilling Program), pp. 1–29.
- Robinson, A., Callow, B., Böttner, C., Yilo, N., Provenzano, G., Falcon-Suarez, I.H., Marin-Moreno, H., Lichtschlag, A., Bayrakci, G., Gehrman, R., Parkes, L., Roche, B., Saleem, U., Schramm, B., Waage, M., Lavayssière, A., Li, J., Jedari-Eyvazi, F., Sahoo, S., Deusner, C., Kossel, E., Minshull, T.A., Berndt, C., Bull, J.M., Dean, M., James, R., Chapman, M., Best, A.I., Bünz, S., Chen, B., Connelly, D.P., Elger, J., Haeckel, M., Henstock, T.J., Karstens, J., Macdonald, C., Matter, J.M., North, L., Reinardy, B., 2021. Multiscale characterisation of chimneys/pipes: Fluid escape structures within sedimentary basins. *Int. J. Greenhouse Gas Control* 106, 103245.
- Sahoo, S.K., Marin-Moreno, H., North, L.J., Falcon-Suarez, I., Madhusudhan, B.N., Best, A.I., Minshull, T.A., 2018. Presence and consequences of coexisting methane gas with hydrate under two phase water-hydrate stability conditions. *J. Geophys. Res.* 123 (5), 3377–3390. <https://doi.org/10.1029/2018JB015598>.
- Sava, D., Hardage, B.A., 2006. Rock physics characterization of hydrate-bearing deepwater sediments. *Leading Edge* 25 (5), 616–619. <https://doi.org/10.1190/1.2202666>.
- Schwalenberg, K., Gehrman, R.A.S., Rippe, D., Bialas, J., 2020. Analysis of marine controlled source electromagnetic data for the assessment of gas hydrates in the Danube deep-sea fan, Black Sea. *Mar. Pet. Geol.* 122, 104650.
- Sinha, M., Patel, P., Unsworth, M., Owen, T., MacCormack, M., 1990. An active source electromagnetic sounding system for marine use. *Mar. Geophys. Res.* 12 (1–2), 59–68.
- Stoker, M. S., Balson, P. S., Long, D. M., Tappin, D. R., 2011. An overview of the lithostratigraphical framework for the Quaternary deposits on the United Kingdom continental shelf. *British Geological Survey, Research Report RR/11/03*.
- Stolt, R., 1978. Migration by Fourier transform. *Geophysics* 43, 23–48.
- Weidelt, P., 2007. Guided waves in marine CSEM. *Geophys. J. Int.* 171, 153–176.
- Weitemeyer, K.A., Constable, S., Tréhu, A.M., 2011. A marine electromagnetic survey to detect gas hydrate at Hydrate Ridge, Oregon. *Geophys. J. Int.* 1–16.
- White, J.E., 1975. Computed seismic speeds and attenuation in rocks with partial gas saturation. *Geophysics* 40 (2), 224–232. <https://doi.org/10.1190/1.1440520>.
- Zhang, X., Sanderson, D.J., 2002. *Numerical Modelling and Analysis of Fluid Flow and Deformation of Fractured Rock Masses*. Elsevier.